Dependence of Plasma-Current Coupling on Current Rise Time in Gas-Puff Z-Pinches

Nicholas A. Aybar, *Member, IEEE*, Fabio Conti, *Member, IEEE*, Marko Cvejić, Dimitri Mikitchuk, Maylis Dozières, Eyal Kroupp, *Member, IEEE*, Jeff Narkis, *Member, IEEE*, Yitzhak Maron, *Fellow, IEEE*, and Farhat N. Beg, *Fellow, IEEE*

***Abstract*—Experiments measuring the azimuthal magnetic field of gas-puff Z-pinch implosions on two drivers of significantly different timescales are presented. Using a Zeeman-based spectroscopic technique, measurements of B_θ are compared with calculated values using Ampere's law and the load current measured by inductive probes to define the "plasma-current coupling." Oxygen gas-puff implosions carried out on the compact experimental system for Z-pinch and ablation research (CESZAR) linear transformer driver (LTD) with a peak current of ∼500-kA and ∼180-ns rise time exhibited substantially lower plasma-current coupling when compared to implosions on the Weizmann Institute of Science (WIS) current driver (300-kA peak and 1600-ns rise), 48% ± 18% and 95% ± 6%, respectively. Potential causes for the significant differences in plasma-current coupling between the two drivers are examined. Shunted current across instability structures present in the CESZAR implosions is ruled out as a source of current loss. The radial charge state distribution is discussed, and a trailing plasma composed of higher charge states is hypothesized to carry a significant portion of the driver current.**

***Index Terms*—Magnetic field measurement, plasma pinch, pulsed power systems.**

I. Introduction

GAS-PUFF Z-pinches are systems in which a fast-opening valve injects gas into the anode–cathode gap of a pulsed power driver. Typically, the discharging pulsed power system supplies current to the gas-puff load, converts the gas into conductive plasma, and drives the cylindrical plasma radially inward with its self-generated magnetic field. When the plasma reaches the central axis, its kinetic energy is thermalized and a hot, dense plasma is produced with many applications, including as a bright X-ray or neutron source [1], [2].

The azimuthal magnetic field driving this process, B_θ, is the most important parameter and information of its evolution and spatial distribution allows Z-pinch models to better capture the various physical processes occurring in Z-pinch implosions. Because the entire Z-pinch implosion is driven by the pulsed current and its associated magnetic field, directing current through the plasma column is necessary to couple driver energy into plasma kinetic energy and subsequently achieve the desired high energy density state of the stagnated plasma. Experimental measurements of B_θ with spatial information are challenging to obtain in dense plasmas; several techniques have been successfully implemented, such as Faraday rotation [2], [3], [4], proton deflectometry [5], [6], and a few variations of Zeeman spectroscopy intended for high-density conditions when Stark broadening smears out the Zeeman splitting pattern [7], [8], [9]. Polarization-based Zeeman spectroscopy can produce local measurements of B_θ at the plasma–vacuum boundary in Stark broadened conditions, allowing current coupling to the imploding plasma to be examined even during the stagnation phase [10]. This technique has been used to study the effect of an external axial magnetic field on the current distribution in imploding plasmas at the Weizmann Institute of Science (WIS) [11]. It was found that when the initial axial magnetic field is applied, a significant portion of the current flows in a low-density plasma, residing radially beyond the dense imploding plasma. Extended magnetohydrodynamic simulations also studied this phenomenon [12]. Later experiments of oxygen gas puffs at WIS using the same pulsed power driver showed that the amount of shunted current in the low-density peripheral plasma is also affected by the conditioning of the electrodes and the location of the Helmholtz coils relative to the electrodes [13], [14].

Z-pinch experiments using polarization-based Zeeman spectroscopy were carried out at UC San Diego to investigate the evolution of the current distribution of such implosions by a fast pulsed power generator compact experimental system for Z-pinch and ablation research (CESZAR). These are compared to the results of a similar experiment performed at WIS for implosions driven by a relatively slow pulsed power generator. The roles of load geometry and pulsed power driver characteristics on plasma-current coupling have not been studied extensively to date. In this article, we use the term "plasma-

Manuscript received 16 December 2021; revised 22 July 2022; accepted 8 August 2022. Date of publication 24 August 2022; date of current version 23 September 2022. This work was supported in part by the Department of Energy Office of Science under Grant DE-SC0019234 and in part by the National Nuclear Security Administration (NNSA) under Award DE NA0003842. The review of this article was arranged by Senior Editor S. J. Gitomer. *(Corresponding author: Nicholas A. Aybar.)*

Nicholas A. Aybar, Fabio Conti, and Farhat N. Beg are with the Center for Energy Research, Department of Mechanical and Aerospace Engineering, University of California San Diego, La Jolla, CA 92093 USA (e-mail: naybar@eng.ucsd.edu).

Marko Cvejić, Eyal Kroupp, and Yitzhak Maron are with the Faculty of Physics, Weizmann Institute of Science, Rehovot 7610001, Israel.

Dimitri Mikitchuk was with the Faculty of Physics, Weizmann Institute of Science, Rehovot 7610001, Israel. He is now with the École Polytechnique Fédérale de Lausanne, 1015 Lausanne, Switzerland.

Maylis Dozières was with the Center for Energy Research, Department of Mechanical and Aerospace Engineering, University of California San Diego, La Jolla, CA 92093 USA. She is now with General Atomics, San Diego, CA 92121 USA.

Jeff Narkis was with the Center for Energy Research, Department of Mechanical and Aerospace Engineering, University of California San Diego, La Jolla, CA 92093 USA. He is now with the Lawrence Livermore National Laboratory, Livermore, CA 94550 USA.

Color versions of one or more figures in this article are available at https://doi.org/10.1109/TPS.2022.3198385.

Digital Object Identifier 10.1109/TPS.2022.3198385

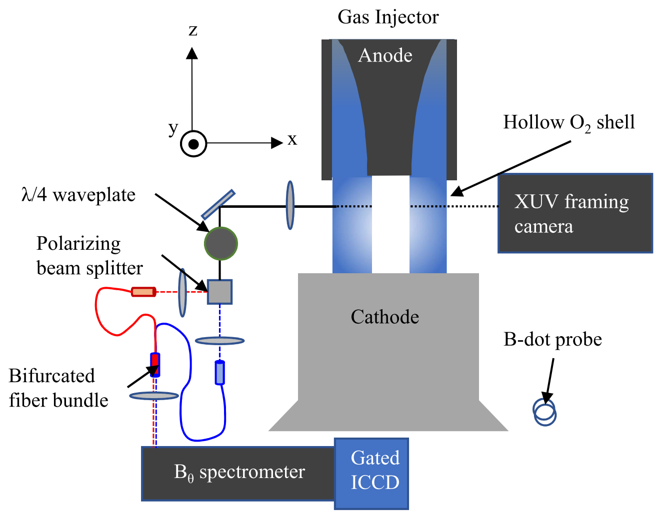

Fig. 1. Diagram of the CESZAR load region and diagnostics arrangement. The spectrometer imaging system and XUV framing camera view the plasma from opposite sides along the same line of sight. The XUV framing camera resolution is ~0.3 mm. The spectrometer system exhibits a spatial resolution of 0.8 mm and a spectral resolution of 0.3 Å.

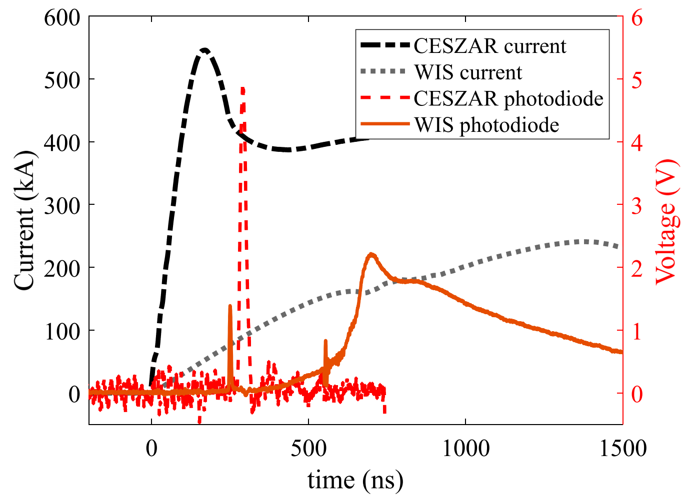

Fig. 2. Current profiles and photodiode response signals for both the CESZAR and WIS drivers. The CESZAR photodiode shown was filtered with a 3-μm Al foil and is sensitive to photon energies between 500 and 1500 eV, though bright K-shell emission for O is expected near 570 eV. The photodiode used on the WIS driver is sensitive to the UV–visible range. Diagnostic trigger signals are also visible on the WIS diode signal near 250 and 550 ns.

current coupling" to describe the quantity of current supplied by the pulsed power driver that is flowing within the imploding plasma.

The CESZAR linear transformer driver (LTD) is a low impedance driver with a peak current of ~500 kA and a quarter period of ~180 ns [15]. The system used at WIS reaches a peak current of ~300 kA in 1600 ns [11]. By comparison to the WIS system, CESZAR reaches a comparable peak current but in nearly 1/10th the time, although the experiments performed at WIS reached stagnation at ~660 ns with a current of ~170 kA at stagnation. The WIS implosions were designed to reach temperatures and charge states during the implosion phase comparable to values expected on the CESZAR driver; this was achieved by using low-mass gas puffs that reach stagnation during the current rise. This communication aims to compare the results obtained from similar experiments on both platforms, explore potential causes for discrepancies, and discuss the implications of using fast-rise LTDs for gas-puff implosions.

II. Experimental Configuration

The CESZAR LTD cavity contains 20 "bricks" arranged in parallel and connected to a conical transmission line leading to the gas-puff load region. Each "brick" consists of two high-voltage capacitors connected in series to a spark-gap switch in between. More details on the CESZAR driver are reported in [15]. For each experimental discharge, the cavity was charged with a dual-polarity voltage of ±60 kV across all 20 bricks resulting in a peak current of ~500 kA. The driver inductance is 18.5 nH, with the load inductance adding ~8 nH. Fig. 1 contains a diagram of the load region and diagnostic arrangement. Three absolutely calibrated differential b-dot probes all located 10 cm from the central axis and 120° from each other azimuthally were used to measure the total circuital current in the load region for each discharge by averaging their integrated signals. Filtered photodiodes were employed to observe the time-resolved emission from the stagnating plasma and determine the experimental stagnation time. The photodiodes are primarily relied on to determine the time of stagnation for each implosion. A typical CESZAR current profile and a photodiode response signal are shown in Fig. 2.

The gas-puff load is produced by an electromagnetic valve opened ~350 μs before the cavity discharge. A complete characterization of the gas-injector performance has been carried out on a separate test chamber. Conti *et al.* [17] detailed this process, which has been repeated using oxygen at the conditions used in the CESZAR experiment. The hollow gas shell produced by the injector contains nearly all the mass between the radii of 1 and 1.9 cm with a peak density at $R \approx 1.3$ cm.

A fast-framing microchannel-plate coupled pinhole camera captured three time-gated images of the plasma self-emission from each discharge in the extreme ultraviolet (XUV) range. For photon energies >25 eV, the spatial resolution is limited at 0.3 mm by geometrical optics. The camera used a gate width of ~5 ns for each frame with a 20-ns interframe delay. The framing camera field of view extends across the entire anode–cathode gap of 14.2 mm.

The spectroscopic system designed to measure the azimuthal magnetic field is similar to those discussed in previous work at various institutions [8], [11], [13], [16]. When emission is viewed parallel to the magnetic field, only the σ components of a given transition are observable. In this configuration, emission from $\sigma+ (\Delta m = m_u - m_l = 1$, where m_u and m_l are the magnetic quantum numbers of the upper and lower states, respectively) and $\sigma- (\Delta m = -1)$ is each circularly polarized with opposite handedness. The optical system converts the circularly polarized light of opposite handedness into orthogonal linearly polarized light with a $\lambda/4$ waveplate. A polarizing beam splitter cube then separates the orthogonal components. The image of each polarization is

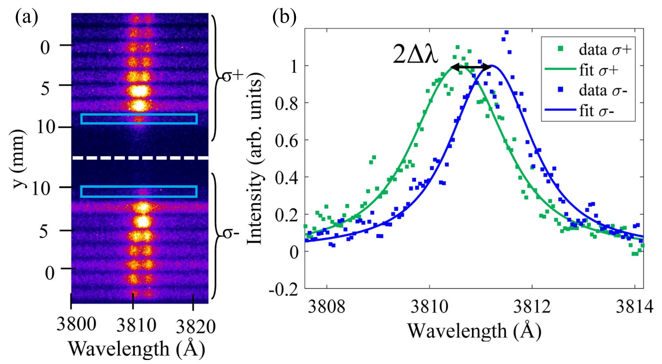

Fig. 3. Spectral image obtained from an O_2 implosion on the CESZAR driver viewing one half of the plasma column and integrating chordally. (a) Top and bottom half contain emission spectra of the O VI line at 3811.35 Å from each leg of the optical system. The blue rectangles represent the region selected for determination of B_θ. Doppler shifts due to the implosion velocity are responsible for the split line profiles observed at small radii in (a). (b) Lineouts together with the Voigt fit to each set of data.

then relayed through a bifurcated fiber bundle to the imaging spectrometer coupled to an intensified charge-coupled device (ICCD) camera. The ICCD gate width was 8 ns. The spectral window observed emission from 3780 to 3830 Å with a spectral resolution of 0.3 Å. The field of view of the entire fiber array, consisting of ten fibers on each leg, ranged from $R = -2$ to 13 mm with each fiber viewing an area $\sim$1 mm across.

An example of the resulting spectral image is shown in Fig. 3, which shows emission from the O VI $3s^3S_{1/2}$–$3p^2P_{3/2}$ transition at 3811.35 Å. Data from both polarization channels are selected at the outer edge of emission where the line of sight is strictly parallel to B_θ, each at the same spatial location. The selected data from each leg are then fit to a Voigt profile to determine the central location of each sample and thus the relative wavelength separation, $2\Delta\lambda$. The Gaussian portion of the Voigt profile accounts for instrumental and thermal Doppler broadening, while the Lorentzian component accounts for the Stark broadening. For the O VI transition, $B_\theta(T) = \Delta\lambda(\text{Å})/0.076$. The spectral window also occasionally observed the O III $3s^3P_2$–$3p^3D_2$ at 3791.26 Å transition for which $B_\theta(T) = \Delta\lambda(\text{Å})/0.09$. The uncertainty of the measurement is defined by the 95% confidence interval based on the Voigt fitting.

The experimental setup used at University of California San Diego (UCSD) followed the same general arrangement as was used at WIS, which is discussed in complete detail in [13]. The key difference between both facilities lies in the design of the pulsed power drivers. The WIS driver consists of 4×4 μF capacitors charged to 24 kV and produces a peak current of $\sim$300 kA with a rise time of 1600 ns, with an implosion time of $\sim$660 ns. The total driver inductance is 62 nH with the load inductance adding $\sim$8 nH. Another potentially significant difference between the two experiments is the electrode geometries. While both systems set the metallic injector nozzles as the anode, the WIS machine design uses a cylindrical knife-edge surrounding a wire mesh as the cathode. By contrast, the CESZAR cathode consists of a honeycomb hole pattern on a flat metallic surface with no knife edge.

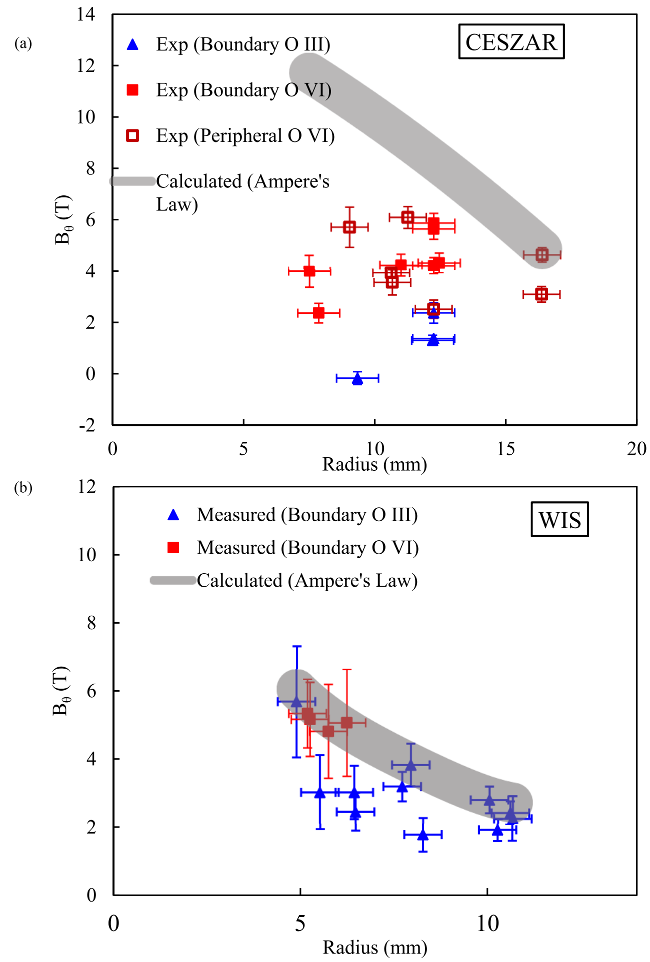

Fig. 4. Results from (a) CESZAR and (b) WIS experiments. The individual data points represent the values of B_θ measured experimentally using line emission from the labeled charge states. For ease of viewing, the range of calculated values corresponding to each measured point is represented by the wide gray curve.

III. Results and Discussion

The spectroscopically determined values of the azimuthal magnetic field for both the CESZAR and WIS experiments are shown in Fig. 4. To examine the plasma-current coupling during the implosions, the measured values of B_θ are shown alongside their corresponding "expected" values, represented by the wide gray curves in Fig. 4. The calculated values are obtained using Ampere's law applied to a cylindrical conductor

$$B_\theta = \mu_0 I / 2\pi r_{\text{spect}} \tag{1}$$

where I is the total current measured by the b-dot probes at the time of the spectroscopic measurement and r_{spect} is the radius at which spectral data are selected. The spectral data are selected at the largest radius possible, which results in a measurement of B_θ where the uncertainty is less than 30%. Experimental results are presented using "pinch-relative" timing, meaning that $t = 0$ ns corresponds to the stagnation time of the experiment, when the peak signal is detected on the photodiodes.

Comparing measured values of B_θ to values calculated with (1) indicates how much driver current is within the plasma at

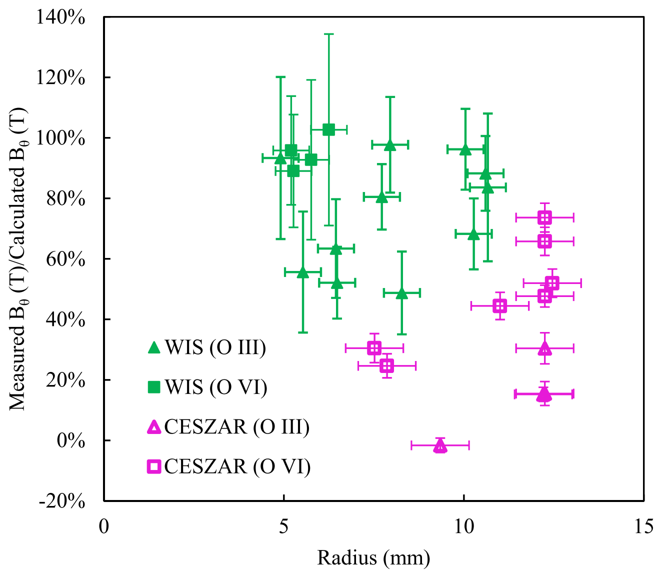

Fig. 5. Ratios of measured/calculated values of B_θ for both WIS and CESZAR experiments. Measurements made from O III emission are displayed as triangles, while O VI are displayed as squares.

the selected radius. It should be noted that, for the purpose of clarity, the "calculated" curves in Fig. 4 are made of a collection of calculated values from separate shots, each corresponding to a measured value; the curves shown therefore do not necessarily exhibit an r^{-1} dependence of B_θ since the current may change rapidly in the implosion. The data shown in Fig. 4(a) labeled "boundary" exclusively contain the results for which r_{spect} coincides with the outer plasma radii as determined by the peak intensity gradient observed with the fast-framing camera (r_{image}), within ± 0.7 mm. Conversely, the data labeled "peripheral" contain data where r_{spect} lies beyond r_{image}. Emission from O VI is sometimes observed extending to radii greater than r_{image} for CESZAR discharges. The observance of the "peripheral" O VI emission varies between shots and does not heavily depend on diagnostic acquisition time. This type of data ($r_{\text{spect}} > r_{\text{image}}$) was not observed in the comparable WIS experiment. Still, Fig. 4(a) shows that for many of these cases, the total circuital current is still not accounted by measurements made using the O VI transition except for the points seen at $\sim$16 mm for which $r_{\text{image}} \approx 7$ mm; these extreme cases were observed at $t = -57$ and -40 ns.

The ratios of the measured values of B_θ to the calculated ones for both WIS and CESZAR experiments are shown in Fig. 5. The results shown therein are exclusively where $r_{\text{spect}} \approx r_{\text{image}}$. While the variation in plasma-current coupling is large in both cases, the CESZAR data clearly fall below the WIS data, with a maximum of $\sim$75% obtained early in the implosion phase at a relatively large radius, while the WIS data consistently exhibit plasma-current coupling near 100% relatively late in the implosion phase when the plasma reaches 5 mm radius. The average plasma-current coupling for WIS was 75% $\pm$ 18% and 95% $\pm$ 6%, for O III and O VI measurements, respectively. The values for CESZAR were 15% $\pm$ 13% and 48% $\pm$ 18% for O III and O VI measurements, respectively.

In contrast to the WIS results, the CESZAR data shown in Fig. 5 show an apparent trend as the implosion progresses. The plasma-current coupling decreases as the implosion progresses toward a smaller plasma radius. This trend is apparent for both data measured with O VI and O III. This means that as the imploding plasma moves radially inward, a significant portion of the current remains at a greater radius, presumably being carried by plasma not "swept up" in the implosion or trailing low-density plasma. This trend may provide a clue in understanding the cause of low plasma-current coupling in the CESZAR experiments. The lack of an inductive notch in the current profile in Fig. 2 is representative of most CESZAR discharges, also indicating that the current is not imploding to a small radius and further justifying the reliance on local spectroscopic measurements of B_θ.

To understand the observed current loss from the imploding plasma driven by the CESZAR current driver, some possible explanations are considered. First, the possibility of current shunting across magneto Rayleigh–Taylor instability (MRTI) structures is examined, and second, the radial charge state distribution is discussed.

One potential explanation may be that the current is shunted across the bubbles formed at the plasma–vacuum boundary due to the MRTI on implosions driven CESZAR. Because of the faster current rise time of the CESZAR experiment, the plasma is accelerated at a significantly greater rate than in the WIS experiment. Average acceleration values calculated using implosion times and velocities obtained via imaging yield approximately $5.4 \pm 2.8 \times 10^8$ km/s^2 on CESZAR and $6.8 \pm 0.5 \times 10^7$ km/s^2 at WIS. This may lead to a greater growth rate γ of the MRTI during the implosion phase given its dependence on g (acceleration) in the following expression for amplitude growth of MRTI perturbation of wavenumber k:

$$\gamma_{\text{MRT}} \propto \sqrt{gk}. \tag{2}$$

The average implosion velocity can be estimated using the three images provided by the XUV framing camera in the CESZAR experiment and is typically between 100 and 150 km/s. Analyzing the Doppler shifted line profiles obtained on CESZAR also yields implosion velocities in the same range. By comparison, the average WIS implosion velocity is near 45 $\pm$ 2.5 km/s. The images also directly provide information of the stability of the plasma–vacuum boundary. An example of the plasma images produced on CESZAR is shown in Fig. 6. Two sets of images from two separate shots are shown in Fig. 6(a)–(c) and (d)–(f). The frames shown in Fig. 6(b) and (d) were acquired during the same window that the spectrographic image is taken; thus, the field of view of the spectrometer is illustrated by the blue circles shown in Fig. 6(b) and (d) with the selected region used to measure B_θ highlighted in green.

The relatively low degree of MRTI development seen in Fig. 6(b) is typical of the CESZAR data presented here where $r_{\text{image}} \approx r_{\text{spect}}$. Even though the CESZAR imploding plasma reaches significantly greater (2–3 times) radial velocities than on the WIS driver, at the time the spectroscopic data are

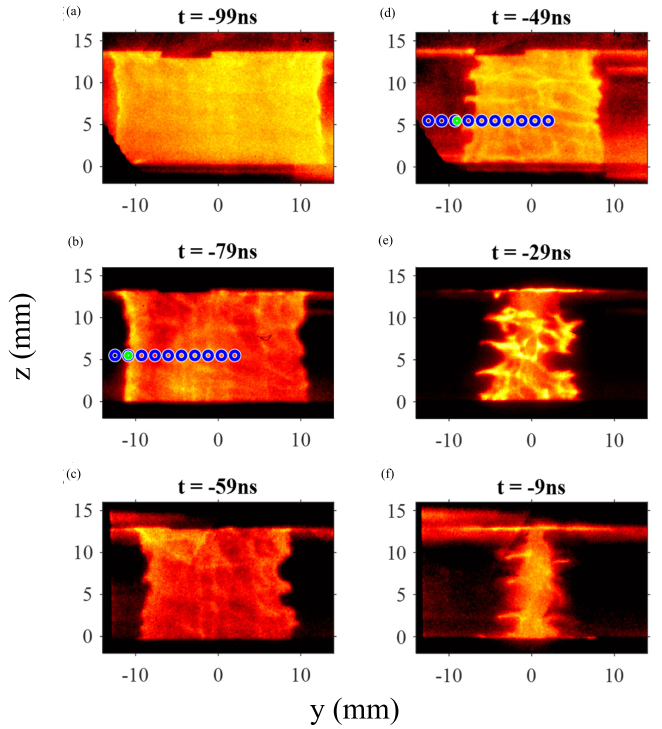

Fig. 6. Time-gated XUV images of a CESZAR O_2 implosion. (a)–(c) and (d)–(f) Separate shots of similar conditions, but with different diagnostic timings. (b) and (d) Each shot of the field of view of each fiber seen by the spectrometer with the blue circles. The region selected for analysis is highlighted in green.

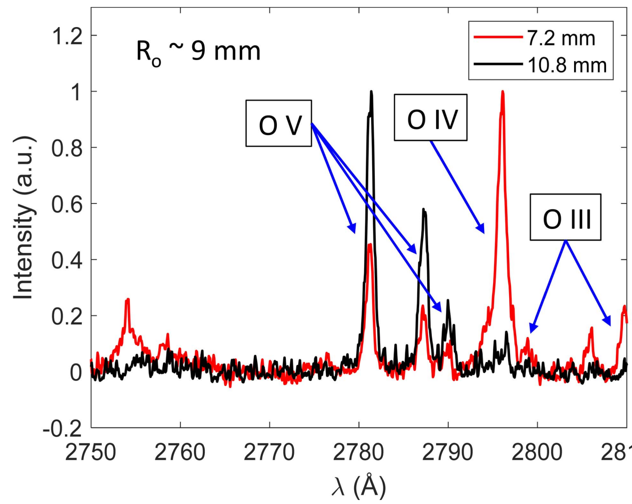

Fig. 7. Radially resolved spectroscopic data obtained from the WIS experiment observing a wider spectral range in the second order. Shown are the spectra taken at two radial positions surrounding the outer plasma radius r_{image} where $r_{\text{image}} = 9.0$ mm. The charge states of the identified spectral lines are displayed.

obtained at r_{image}, the MRT instability has not yet substantially grown. While the WIS data discussed here exhibit a higher degree of stability than the CESZAR results shown, recent work of a separate similar experiment discussed in [16] as well as earlier work shown in [7] exhibit a high degree of MRTI and strong axial gradients or flaring; yet, measurements of B_θ at the outer plasma boundary (r_{image}) still show close to 100% plasma-current coupling. Each of these comparable experiments used a slower rising current driver than CESZAR (500 kA in 500 ns and 320 kA in 620 ns).

However, where $r_{\text{spect}} > r_{\text{image}}$, later in the CESZAR implosions, MRT instability structures have grown substantially and are shown in Fig. 6(d)–(f). In this case, emission from O VI remains beyond the MRT structures and B_θ measurements there yield plasma-current coupling near 50%. Therefore, the relatively low plasma-current coupling observed on the CESZAR driver cannot be attributed to shunting across MRTI structures.

A second time-gated spectrometer with a greater spectral range (2750–2850 Å) was also employed during the WIS experiment. When only O III was observed with the B_θ spectrometer, this wide-range spectrometer often observed emission from O IV and O V just beyond the bulk plasma radius and just beyond where the B_θ measurement could be made using the O III transition observed with the B_θ spectrometer. Fig. 7 shows an example of such a case, where $r_{\text{image}} = r_{\text{spect}} = 9$ mm, and yet, emission lines from O V were observed up to ∼11 mm. When low plasma-current coupling is measured via an O III transition, this plasma consisting of higher charge states residing beyond r_{image} presumably carried a substantial fraction of the total current.

For both experiments, a radial charge state distribution is observed such that higher charge states reside at larger radii. This is apparent in the WIS experiment both on the B_θ spectrometer and the wide-range spectrometer. On CESZAR, the emission from O III is always observed at a smaller radius than where O VI is observed. Given the greater current level reached in shorter times in the CESZAR experiment, we can expect to reach higher temperatures and, therefore, higher ionization states in CESZAR implosion than in WIS implosion. This is consistent with the fact that emission from O VI appears relatively early in the CESZAR implosions, as early as 100 ns prior to stagnation, contrasted with 30 ns prior to stagnation in WIS implosions. In this case, it is plausible that even higher charge states are present in the CESZAR implosions that are not observable with the spectroscopic system.

Line ratios observed in the WIS experiment indicate an imploding plasma electron temperature T_e of 3–10 eV with 10 eV being a sufficient temperature to produce a fraction of plasma ionized to O VI. The values were obtained by matching experimental spectra to synthetic spectra from the Saha-LTE tool on the NIST Atomic Spectra database with electron density, $n_e = 10^{17}$ cm^{-3} [18]. Conversely, simulation run using the collisional-radiative code FLYCHK indicates that O VII may make up a substantial portion of the ionization distribution at just 16 eV [19], which may be achieved during the CESZAR implosion phase. The expected ion distributions for given electron temperatures and emission spectra in the range of the imaging diagnostic are shown in Fig. 8. At temperatures above 12 eV, emission from O VI is expected to dominate the spectral range detectable by the XUV framing camera, with the peak intensity near 70 eV in photon energy based on

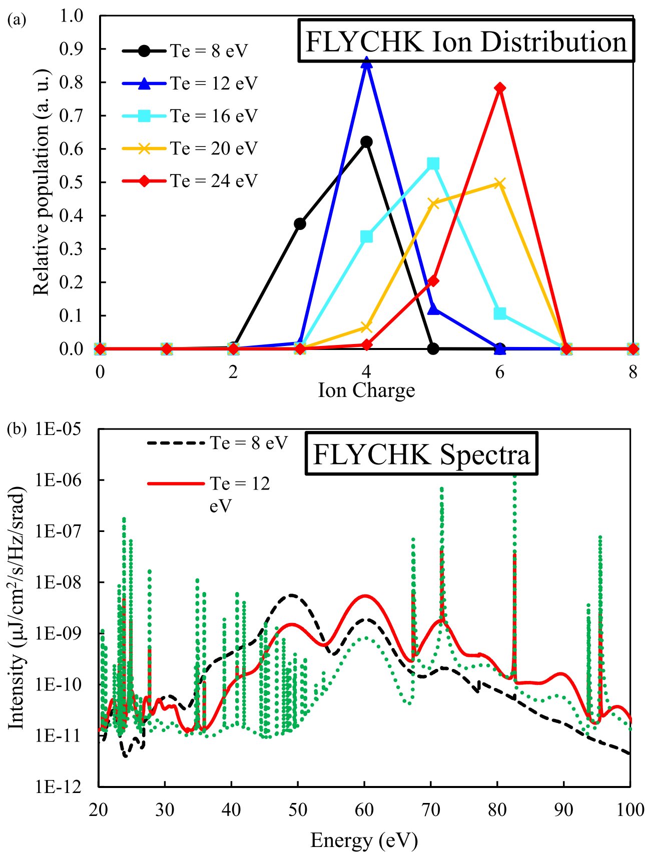

Fig. 8. (a) Ion distributions for given electron temperatures estimated in FLYCHK using an electron density of 10^{17} cm^{-3}. (b) Emission spectra for three temperatures. The peak emission for $T_e = 8$ eV appears near 50 eV and results from O IV emission, while the peak emission for both $T_e = 12$ and 24 eV appears between 70 and 80 eV and results from O VI emission.

FLYCHK simulations; O VI emission is expected to dominate still at higher temperatures even when higher charge states are abundant ($T_e > 20$ eV), predominantly O VII. This means that both the spectroscopic and imaging diagnostic systems may be unable to detect emissions from higher charge states if T_e is sufficiently high.

Without a dedicated wide-range spectrometer to observe higher charge states or determine electron temperature, we cannot be certain that nearby higher charge states are responsible for the "missing" current in the CESZAR implosions. However, given the higher charge states observed on CESZAR relatively early in the implosion and the trend toward decreasing plasma-current coupling as the implosion progresses, trailing plasma composed of higher charge states undetectable by the diagnostics used remains the most likely explanation since a current path at a larger radius is favorable due to the reduced inductive impedance. Considering the Spitzer resistivity model ($\eta \propto T^{3/2}$), this means that the larger radius current path is also favorable due to a relatively lower resistivity since the higher charge states are likely accompanied by higher temperatures [20]. It is also important to note that the observed trailing O VI exhibits similar line broadening to emission at the bulk plasma boundary, indicating a similar density of each region. At present, further investigation is required to discriminate the relative importance of each of these factors in the behavior of the current.

In addition, we recognize that the electrode geometry may play a role in the plasma-current coupling during the implosion as it may impact the breakdown phase. The knife-edge cathode geometry used on the WIS experiment may facilitate the initial gas breakdown, while a flat, honeycomb cathode was used on the CESZAR experiment. A flat electrode may be responsible for a poor initial gas breakdown, which may lead to unswept or trailing plasma that may shunt current during the implosion. This mechanism for shunted current may also explain the relatively high rate of shot failure observed on the CESZAR driver. Oxygen discharges on the CESZAR driver often fail to implode and show evidence of a failed dielectric breakdown at the start of the current pulse. Because of this fact, it is reasonable to suspect nonuniform or incomplete ionization during "successful" Z-pinch shots. Furthermore, the initial gas density profile and injector flow characteristics may impact current coupling as well. Giuliani *et al.* [21] discussed the effect of initial breakdown on implosion dynamics up to the stagnation phase. These potential issues, specifically, the effect of the electrode structure, initial gas density profile, and their interaction on the initial breakdown phase of the CESZAR driver will be examined in a future publication.

IV. Conclusion

Two gas-puff Z-pinch experiments were carried out using current drivers of significantly different current rise rates. Experiments on the faster rising current driver, CESZAR, exhibit relatively low plasma-current coupling when compared to the slower rising current driver at WIS. Measurements of the azimuthal magnetic field were made in both experiments and compared with calculated values to determine the degree of "plasma-current coupling" exhibited by both experimental systems. In contrast to the results produced by the WIS driver, the CESZAR data show substantially lower levels of plasma-current coupling, typically near 50%.

Examination of the stability of the imploding plasma column shows that the current shunting across instability structures is not a likely cause of the reduced plasma-current coupling. A trailing plasma composed of higher charge states, namely, O VI, was intermittently observed at greater radii than the bulk imploding plasma column. While this trailing plasma was sometimes found to carry most of the driver current, the measured values of B_θ often fell short of the values calculated by Ampere's law at those radii. The trailing plasma may be a result of a nonuniform or incomplete dielectric breakdown of the oxygen gas in the initial stage of the CESZAR current pulse, which allows for a low inductance current path across the anode–cathode gap.

Collisional-radiative atomic kinetic simulations of the expected plasma state indicate that O VII may be present in the imploding plasma. However, the diagnostics employed in the CESZAR experiments are not expected to observe these higher charge states as O VI is the dominant emitter for the spectral bands observed by the diagnostics. Full characterization of the radial charge state distribution and T_e of the imploding plasma may provide insight into the expected current distribution evolution between the two drivers. Further work involving modeling of the plasma implosion is necessary to study this behavior.

REFERENCES

[1] M. G. Haines, "A review of the dense Z-pinch," *Plasma Phys. Controlled Fusion*, vol. 53, no. 9, Jun. 2011, Art. no. 093001, doi: 10.1088/0741-3335/53/9/093001.

[2] J. L. Giuliani and R. J. Commisso, "A review of the gas-puff Z-pinch as an X-ray and neutron source," *IEEE Trans. Plasma Sci.*, vol. 43, no. 8, pp. 2385–2453, Aug. 2015, doi: 10.1109/TPS.2015.2451157.

[3] S. N. Bland *et al.*, "Use of Faraday probing to estimate current distribution in wire array Z pinches," *Rev. Sci. Instrum.*, vol. 77, no. 10, Oct. 2006, Art. no. 10E315, doi: 10.1063/1.2227443.

[4] V. V. Ivanov, A. A. Anderson, D. Papp, A. L. Astanovitskiy, V. Nalajala, and O. Dmitriev, "Study of magnetic fields and current in the Z pinch at stagnation," *Phys. Plasmas*, vol. 22, no. 9, Sep. 2015, Art. no. 092710, doi: 10.1063/1.4931079.

[5] V. Munzar *et al.*, "Investigation of magnetic fields in Z-pinches via multi-MeV proton deflectometry," *IEEE Trans. Plasma Sci.*, vol. 46, no. 11, pp. 3891–3900, Nov. 2018, doi: 10.1109/TPS.2018.2874207.

[6] D. Mariscal *et al.*, "Measurement of pulsed-power-driven magnetic fields via proton deflectometry," *Appl. Phys. Lett.*, vol. 105, no. 22, Dec. 2014, Art. no. 224103, doi: 10.1063/1.4902982.

[7] G. Davara, L. Gregorian, E. Kroupp, and Y. Maron, "Spectroscopic determination of the magnetic-field distribution in an imploding plasma," *Phys. Plasmas*, vol. 5, no. 4, pp. 1068–1075, Apr. 1998, doi: 10.1063/1.872637.

[8] R. P. Golingo, U. Shumlak, and D. J. Den Hartog, "Zeeman splitting measurements in a high-temperature plasma," *Rev. Sci. Instrum.*, vol. 81, no. 12, Dec. 2010, Art. no. 126104, doi: 10.1063/1.3509400.

[9] S. Tessarin *et al.*, "Beyond zeeman spectroscopy: Magnetic-field diagnostics with stark-dominated line shapes," *Phys. Plasmas*, vol. 18, no. 9, Sep. 2011, Art. no. 093301, doi: 10.1063/1.3625555.

[10] G. Rosenzweig, E. Kroupp, A. Fisher, and Y. Maron, "Measurements of the spatial magnetic field distribution in a Z-pinch plasma throughout the stagnation process," *J. Instrum.*, vol. 12, no. 9, Sep. 2017, Art. no. P09004, doi: 10.1088/1748-0221/12/09/P09004.

[11] D. Mikitchuk *et al.*, "Effects of a preembedded axial magnetic field on the current distribution in a Z-pinch implosion," *Phys. Rev. Lett.*, vol. 122, no. 4, Feb. 2019, Art. no. 045001, doi: 10.1103/PhysRevLett.122.045001.

[12] C. E. Seyler, "Axial magnetic flux amplification in Hall-magnetohydrodynamic simulations of externally magnetized Z-pinches," *Phys. Plasmas*, vol. 27, no. 9, Sep. 2020, Art. no. 092102, doi: 10.1063/5.0011833.

[13] N. Aybar *et al.*, "Azimuthal magnetic field distribution in gas-puff Z-pinch implosions with and without external magnetic stabilization," *Phys. Rev. E, Stat. Phys. Plasmas Fluids Relat. Interdiscip. Top.*, vol. 103, no. 5, May 2021, Art. no. 053205, doi: 10.1103/PhysRevE.103.053205.

[14] M. Cvejić *et al.*, "Self-generated plasma rotation in a Z-pinch implosion with preembedded axial magnetic field," *Phys. Rev. Lett.*, vol. 128, no. 1, Jan. 2022, Art. no. 015001, doi: 10.1103/PhysRevLett.128.015001.

[15] F. Conti *et al.*, "MA-class linear transformer driver for Z-pinch research," *Phys. Rev. Accel. Beams*, vol. 23, no. 9, Sep. 2020, Art. no. 090401, doi: 10.1103/PhysRevAccelBeams.23.090401.

[16] G. Rosenzweig *et al.*, "Local measurements of the spatial magnetic field distribution in a Z-pinch plasma during and near stagnation using polarization spectroscopy," *Phys. Plasmas*, vol. 27, no. 2, Feb. 2020, Art. no. 022705, doi: 10.1063/1.5126934.

[17] F. Conti *et al.*, "Characterization of a liner-on-target gas injector for staged Z-pinch experiments," *IEEE Trans. Plasma Sci.*, vol. 46, no. 11, pp. 3855–3863, Nov. 2018, doi: 10.1109/TPS.2018.2856748.

[18] National Institute of Standards and Technology. (2017). *Atomic Spectral Database*. [Online]. Available: nist.gov/pml/atomic-spectra-database

[19] H.-K. Chung, M. H. Chen, W. L. Morgan, Y. Ralchenko, and R. W. Lee, "FLYCHK: Generalized population kinetics and spectral model for rapid spectroscopic analysis for all elements," *High Energy Density Phys.*, vol. 1, no. 1, pp. 3–12, Dec. 2005, doi: 10.1016/j.hedp.2005.07.001.

[20] R. S. Cohen, L. Spitzer, and P. M. Routly, "The electrical conductivity of an ionized gas," *Phys. Rev.*, vol. 80, no. 2, pp. 230–238, Oct. 1950, doi: 10.1103/PhysRev.80.230.

[21] J. L. Giuliani *et al.*, "Effective versus ion thermal temperatures in the Weizmann Ne Z-pinch: Modeling and stagnation physics," *Phys. Plasmas*, vol. 21, no. 3, Mar. 2014, Art. no. 031209, doi: 10.1063/1.4865223.